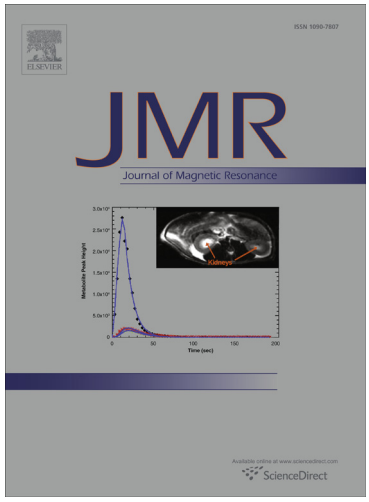

An Optimised Detector For In-Situ High-Resolution NMR In Microfluidic Devices

Graeme Finch, Ali Yilmaz, Marcel Utz

PII: S1090-7807(15)00299-2
DOI: http://dx.doi.org/10.1016/j.jmr.2015.11.011
Reference: YJMRE 5764

To appear in: *Journal of Magnetic Resonance*

Received Date: 16 September 2015
Revised Date: 24 November 2015
Accepted Date: 25 November 2015

Please cite this article as: G. Finch, A. Yilmaz, M. Utz, An Optimised Detector For In-Situ High-Resolution NMR In Microfluidic Devices, *Journal of Magnetic Resonance* (2015), doi: http://dx.doi.org/10.1016/j.jmr.2015.11.011

An Optimised Detector For In-Situ High-Resolution NMR In Microfluidic Devices

Graeme Finch, Ali Yilmaz, and Marcel Utz

School of Chemistry, University of Southampton, Southampton, SO17 1BJ, United Kingdom

Abstract

Integration of high-resolution nuclear magnetic resonance (NMR) spectroscopy with microfluidic lab-on-a-chip devices is challenging due to limited sensitivity and line broadening caused by magnetic susceptibility inhomogeneities. We present a novel double-stripline NMR probe head that accommodates planar microfluidic devices, and obtains the NMR spectrum from a rectangular sample chamber on the chip with a volume of 2 μl. Finite element analysis is used to jointly optimise the detector and sample volume geometry for sensitivity and RF homogeneity. A prototype of the optimised design has been built, and its properties have been characterised experimentally. The performance in terms of sensitivity and RF homogeneity closely agrees with the numerical predictions. The system reaches a mass limit of detection of 1.57 nMol $\sqrt{\text{s}}$, comparing very favourably with other micro-NMR systems. The spectral resolution of this chip/probe system is better than 1.75 Hz at a magnetic field of 7 T, with excellent line shape.

Keywords: NMR, Probes, Stripline, Microfluidics, Transmission Line

1. Introduction

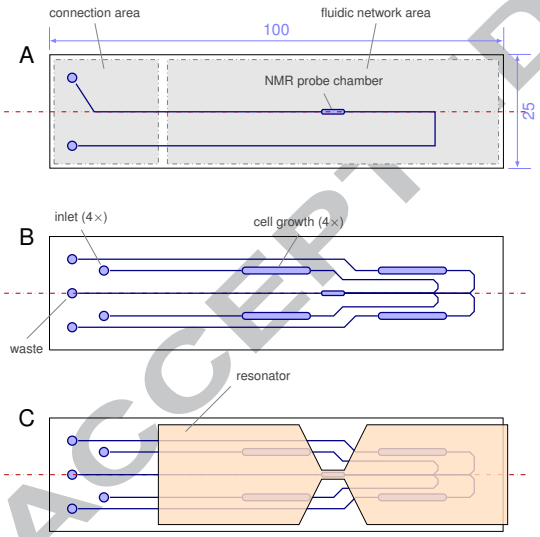

Figure 1: Microfluidic LoC devices (dimensions in mm). A) simple design with a 2 μl sample chamber and access points; B) more complex design with four separate chambers for cell growth and a single sample chamber; C) alignment of the LoC device with the transtmission line resonator.

Microfluidic devices are widely applied in the life sciences, offering a convenient platform for integrating complex biochemical functionality in a compact and expendable package. In particular, they provide very tightly controlled and tailored environments for the culture of cells [1, 2], tissues [3], and small organisms [4]. In principle, NMR spectroscopy would complement such systems very well, enabling non-destructive and non-invasive observation of metabolic processes over a period of time. However, integration of microfluidic systems with NMR spectroscopy presents a number of technical challenges. Conventional liquid-state NMR spectroscopy is mostly done in 5 mm sample tubes, on probe volumes between 200 and 800 μl. Commonly, Alderman-Grant resonators or saddle coils with diameters ranging from 4 to 12 mm and lengths of 8 to 15 mm are used in commercial liquid state NMR probes for excitation and detection. By contrast, microfluidic lab-on-a-chip (LoC) devices are extended planar networks of channels and chambers; two simple examples are shown in Fig. 1A and B. While the overall size of such LoC devices is similar (several cm) to that of conventional NMR detection coils, the volumes contained in their channels are two orders of magnitude smaller. Simply inserting an LoC device into a standard probe (assuming it can be made small enough to physically fit) therefore leads to very low filling factors, and correspondingly poor sensitivity.

A variety of planar micro-NMR detector geometries that are compatible with microfluidic devices have been proposed [5, 6], including planar spiral coils [7, 8], micro-slots [9], Helmholtz pairs [10], and phased array detectors [11, 12].

As is well known, miniaturised NMR detectors benefit from a favorable scaling of mass sensitivity (the absolute number of spins required for a detectable signal) with probe volume [13]. This had led to flow probes with very high sensitivity based on micro-solenoid coils wound around glass capillaries. More recently, capillary detectors have been combined with microfluidic devices to form remote-detection systems, in which a large coil is used for spin excitation and encoding, and signals are detected downstream from liquid flowing out of the chip into a capillary NMR detector [14]. While this is an elegant approach, it requires a fluidic connection between the LoC and the NMR

system, and is therefore not an in-situ technique.

Van Bentum *et al.* [15, 16] have demonstrated the excellent sensitivity and both high B_0 and B_1 homogeneity offered by planar transmission line resonators. These designs are characterised by a planar conductor which is aligned with the static magnetic field symmetrically in between two ground planes. They accommodate a standing electromagnetic wave with a magnetic field anti-node at the centre and nodes at the ends. A constriction at the location of the magnetic field anti-node leads to a concentration of the radio-frequency magnetic field at the location of the sample. While several applications of this type of resonators as flow probes have been described, it has not, to our knowledge, been adapted to accommodate exchangeable microfluidic devices.

In the present contribution, we describe an NMR probe assembly based on a variant of the planar transmission line resonator that accommodates a generic microfluidic chip of dimensions 100 × 25 × 0.8 mm ($l \times w \times h$). The probe (cf. Fig. 2) is designed such that the radio frequency magnetic field is concentrated on a rectangular sample chamber of approximately 1 mm width and 5 mm length in the centre of the chip. With a chamber thickness of 400 μm, this corresponds to a sample volume of 2 μl. The combined design of the probe and the chip has been optimised for sensitivity and for homogeneity of the RF magnetic field by finite element analysis (FEA) of the first resonant electromagnetic eigenmode. A prototype of the probe was built, and its performance characterised by NMR. As will be discussed in detail below, the resulting sensitivity is sufficient to quantify sub-millimolar species within a few tens of minutes of measurement time at a static magnetic field strength of 7 T.

2. Theory and Simulation

As has been shown by Hoult and Richards [17], the sensitivity of NMR detectors (i.e., number of spins precessing within a unit bandwidth for a given signal to noise ratio) is related to their efficiency (i.e., amplitude of the resonant B_1 field per square root of the radiofrequency power delivered to them). Optimisation of one quantity therefore automatically also optimises the other.

In the present work, we have used a finite element analysis approach in order to compute the radiofrequency magnetic and electrical fields in the planar transmission line resonator. This model is based on the Helmholtz equation for the electric field $\mathbf{E}$:

$$\nabla^2\mathbf{E} = \mu\epsilon\frac{\partial^2\mathbf{E}}{\partial t^2} + \mu\sigma\frac{\partial\mathbf{E}}{\partial t}, \tag{1}$$

where μ, ϵ, and σ represent the local magnetic permeability, electrical permittivity, and electrical conductivity, respectively. Since we are only interested in stationary (standing wave) solutions, the time- and spatial dependence of the electric field can be separated as

$$\mathbf{E}(\mathbf{r}, t) = \Re(\mathbf{E}(\mathbf{r})e^{-\lambda t}), \tag{2}$$

with the eigenvalue $\lambda = \delta - i\omega$, and the Helmholtz equation becomes

$$\nabla^2\mathbf{E}(\mathbf{r}) = (\lambda^2\mu\epsilon - i\lambda\mu\sigma)\mathbf{E}(\mathbf{r}), \tag{3}$$

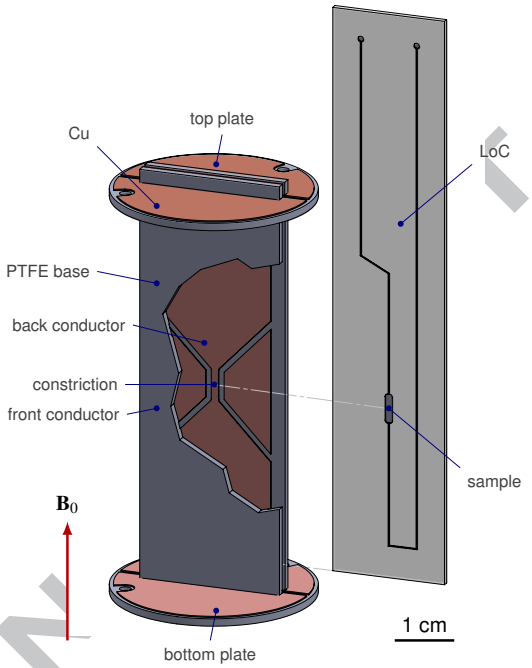

Figure 2: CAD drawing of the transmission line resonator with a corresponding microfluidic LoC device. A part of the front conductor plate has been removed to reveal the constriction at the location of the sample, and the LoC device has been displaced to the right for clarity.

where $\mathbf{E}(\mathbf{r})$ is the complex (magnitude and phase) amplitude of the electric field. FEA modelling of a resonator consists in solving the above non-linear eigenvalue problem given a spatial distribution of the electric conductivity, magnetic permeability, and electric permittivity. Assuming such a solution is found, the complex eigenvalue $\lambda_k = \delta_k - i\omega_k$ then characterises the resonant frequency ω_k as well as the damping coefficient δ_k of the k-th resonant mode (typically, only the fundamental mode is of interest in NMR detectors.) The magnetic field is separated in the same way as the electric field:

$$\mathbf{B}(\mathbf{r}, t) = \Re(i\mathbf{B}(\mathbf{r})e^{-\lambda t}). \tag{4}$$

Faraday's law can then be used to calculate the corresponding magnetic field distribution:

$$\mathbf{B}_k(\mathbf{r}) = \frac{1}{i\lambda_k}\nabla\times\mathbf{E}_k(\mathbf{r}) = \frac{\omega_k - i\delta_k}{\omega_k^2 + \delta_k^2}\nabla\times\mathbf{E}_k(\mathbf{r}). \tag{5}$$

This definition ensures that the magnetic and electric field distributions $\mathbf{E}_k$ and $\mathbf{B}_k$ can both be chosen to be real in the limit of a loss-free system, while the true time-dependent electric and magnetic fields $\mathbf{E}(\mathbf{r}, t)$ and $\mathbf{B}(\mathbf{r}, t)$ are out of phase by $\pi/2$.

The quality factor

$$Q_k = \frac{\omega_k}{2\delta_k} \tag{6}$$

represents the ratio of the stored to the disspated energy per oscillation cycle. Therefore, the time-averaged loss power P_L can be computed from the maximum stored magnetic or electric

energy and Q_k as

$$\bar{P_L} = \frac{\omega_k}{Q_k} \int \frac{1}{2\mu} \mathbf{B}_k \cdot \mathbf{B}_k^{\dagger} \, \mathrm{d}\mathbf{r}. \tag{7}$$

By the correspondence principle, the sensitivity of a resonator tuned to the Larmor frequency is related to the normalised magnetic field

$$\tilde{\mathbf{B}}_k(\mathbf{r}) = \frac{\mathbf{B}_k(\mathbf{r})}{\sqrt{P_L}}. \tag{8}$$

Transmission line resonators were simulated by finding numerical simulations to the eigenvalue equation (3). The geometry of the model is shown in Fig. 3. The conductor plates forming the resonator are represented by an impedance boundary condition, with the electric and magnetic fields excluded from the interior of the conductors [18, p 33], [19, 20]. This type of boundary condition constrains mutually perpendicular components of the magnetic and electric fields in the boundary to be proportional, with the ratio given by the surface impedance

$$Z_s \approx (1 + i) \sqrt{\frac{\omega\mu}{2\sigma}},$$

where σ denotes the bulk conductivity. This eliminates the need to explicitly account for the exponential drop of the electric field within the skin depth, and greatly reduces the number of spatial elements needed for converged results. Due to the symmetry of the system, it is sufficient to explicitly represent only the quadrant $x \geq 0$, $y \geq 0$, corresponding to one lateral half of one conductor. The central plane (yz) between the conductor plates can be represented by a perfect electric conductor (PEC) boundary condition, since the electric and magnetic fields are perpendicular and parallel to it by symmetry, respectively. For the middle plane through the conductors (xz), the inverse is true: the magnetic field is perpendicular to it, while the electric field is parallel. This type of boundary condition is commonly referred to as a perfect magnetic conductor (PMC).

In practice, the resonator geometry is chosen to ensure an eigenfrequency close to, but somewhat above, the Larmor frequency. Fine-tuning is then achieved by adding small capacitances in parallel to the transmission line at the top and bottom plates (Fig. 2). In the finite element simulations, these tuning capacitances were not explicitly modelled, but represented by lumped element boundary conditions at the end planes of the transmission line.

While a perfectly conservative resonator would be characterised by an imaginary eigenvalue λ_k and an infinite Q-factor, several sources of electromagnetic losses limit the attainable values of Q in practice. In the present model, we have taken into account the finite conductivity of the copper plates, the complex electric permittivity of the dielectric between the conductors, and the dissipation factor of the tuning capacitances. Table 1 lists the parameters that were used in the calculations.

3. Experimental

Microfluidic chips were manufactured by cutting preconfectioned PMMA sheets (Nitto Jushi Kogyo Co. Ltd., Tokyo, Japan) with a CO_2 laser cutting system (Epilog, Golden, Colorado USA). The fluidic layer was cut from 0.2 mm PMMA, and was sandwiched between two 0.2 mm PMMA panels using adhesive tape (Thorlabs, Newton, New Jersey, USA) to bond the layers.

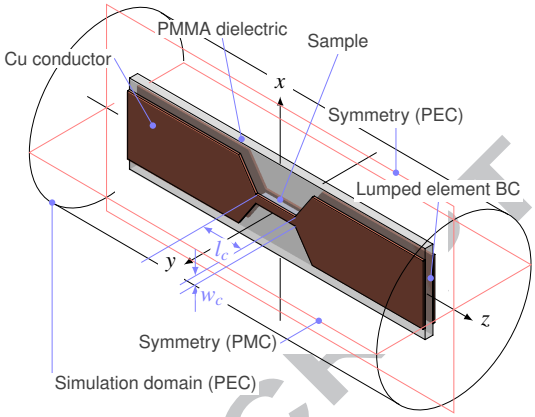

Figure 3: The model used to simulate the chosen geometry. One quarter of the model was defined explicitly and the remainder generated by symmetry using appropriate boundary conditions.

Optimised planar transmission line design was fabricated from single-sided copper-laminated Teflon with a copper thickness of 18 μm (Shenzhen Meidear Co. Ltd., Shenzhen, China). A channel in the copper layer was milled using a micro miller with CNC control (Proxxon, Föhren, Germany) to create the constricted section. The pieces were then cut out from the sheet material using the same milling tool and fixed using cyanoacylate glue (Henkel, UK). The detector was tuned using fixed ceramic capacitors (Johanson, Camarillo, California, USA) and attached to an existing probe base (Bruker, Billerica, Massachusetts, USA).

Finite element simulations were carried out using COMSOL Multiphysics (COMSOL Inc, Cambridge, UK) using the radio frequency (RF) package. The geometry was represented using an unstructured tetrahedral mesh, with the distance between mesh vertices no more than a quarter of the width of the constricted section in the vicinity of the sample area. Self-resonance frequencies and quality factors were calculated using an iterative eigenfrequency solver.

In order to measure their unloaded resonance characteristics, resonator prototypes were weekly coupled between the ports of a vector network analyser (Agilent, Santa Clara, USA). Eigenfrequency and Q factors were measured from the position and 3 dB points of the peak observed in the S_{12} scattering parameter. The Q values were corrected for finite coupling [18, pp 305f].

NMR spectra were acquired on a Bruker AVANCE III spectrometer equipped with a 7 T Oxford Instruments Magnet. Spectra were obtained with a simple 90° pulse-observe sequence, or in some cases with solvent presaturation and a 128 ms T_2 filter consisting of a spin echo train with suppressed J evolution [21]. All NMR data was processed using Math-

ematica. 1D spectra were recorded with a spectral width of 500 Hz, 32k data points and a relaxation delay of 3 seconds between scans. Test samples were made from 150 mM sodium acetate (Sigma Aldrich) in H_2O, and from Dulbecco Modified Eagle's Medium (DMEM) supplemented with 10% Fetal Bovine Serum (FBS) (Life Technologies, USA). 10 mM 4,4-dimethyl-4-silapentane-1-sulfonic acid (Sigma Aldrich) was added as a chemical shift reference.

4. Results and Discussion

4.1. Validation of the FEA Model

The finite element model for planar transmission line resonators was validated by computing the resonance frequencies and quality factors for a range of different resonator geometries, and comparing them to experimental values obtained from prototypes built to nominal geometries from printed circuit board. Resonance frequencies and unloaded Q factors were obtained using a vector network analyser as described in the experimental section. Fig. 4 shows the calculated normalised magnetic field $\tilde{B}_x$ distributions at the centre planes of resonators with outside dimensions of 75 mm $\times$ 20 mm, and 1 mm separation. The constriction area is 20 mm^2 in all cases, but the aspect ratio of the constriction is varied from left to right, with the constriction lengths indicated in the figure. The magnetic field amplitude of the first eigenmode, normalised to 1 W of power disspation, at the central plane between the resonator plates is shown in Fig. 4. As can be seen clearly in the figure, the maxmimum magnetic field amplitude increases at first with the aspect ratio of the constriction, and reaches its highest value in the case of $l_c = 10$ mm. It should be noted that these computations simulated the free resonators, i.e., there were no capacitors at the ends. As a result, the frequency of the first eigenmode monotonously decreases with increasing aspect ratio, due to the increasing inductance of the structure. The simulated eigenfrequencies, compiled in the top panel of Fig. 5 (open triangles), are in excellent agreement with the experimental results (filled triangles).

A second set of resonators were built, tested, and simulated. In this series, the aim was to use additional capacitors between the ends of the resonator conductors in order to keep the resonance frequency close to a target of 300 MHz. The necessary capacitor values were determined empirically. The same capacitance values were then represented in the finite element models as impedance boundary conditions at the end caps (cf. Fig. 3). As shown in Fig. 5 (open and filled circles), the agreement is reasonably good in all cases, with the simulations systematically overestimating the resonance frequency by a small amount.

Computed and measured Q_0 factors for the tuned resonators are compared in the bottom panel of Fig. 5. The simulations initially significantly overestimate Q_0 ($\otimes$). However, these computations assumed the end capacitors to be loss-free, and the only sources of dissipation were the finite conductivity of copper and the loss tangent of the dielectric. The predicted Q_0 values reach from 150 for a 20 mm $\times$ 1 mm ($l_c \times w_c$) constriction up to 310 in the case of 5 mm $\times$ 4 mm. This is not consistent with the measured values, which are constant at about 120 within the measurement accuracy (solid circles). However, the agreement is excellent if a complex boundary impedance $Z_{\mathrm{end}} = (\tan\delta - i)/(\omega C_{\mathrm{end}})$, including a realistic loss tangent $\tan\delta = 0.005$, is used to represent the end capacitors.

To summarise these results: it has been established that the FEA model provides a quantitative prediction of resonance frequencies and quality factors, taking into account resistive as well as dielectric losses. The absolute accuracy of these predictions is of the order of 5%.

4.2. Optimisation

The FEA model was used in order to identify an optimal geometry of the resonator as well as the sample chamber. As is well known, the mass sensitivity of NMR detectors tends to improve as the detector volume is made smaller. Therefore, the sample volume was kept fixed at 2 μl. The thickness of the sample chamber, as well as the separation of the two resonator planes were also kept fixed due to fabrication limitations for the microfluidic chips, which were laminated from PMMA sheets and adhesive tapes of given thickness. The free optimisation variables were therefore: the length of the sample chamber l_s, the length and width of the resonator constriction l_c and w_c, and the terminating capacitances at the end points C_{end}.

The optimisation objective was derived from the first and the second moment of the $\tilde{B}_x$ distribution:

$$O_1 = \frac{\langle \tilde{B}_x \rangle}{\mathrm{mT}/\sqrt{\mathrm{W}}} \quad \text{and} \quad O_2 = \sqrt{\frac{\langle B_x^2 \rangle}{\langle B_x \rangle^2} - 1},$$

where the angular brackets indicate averaging over the sample volume. The overall optimisation objective was a linear combination of O_1 and O_2

$$O = O_1 - \alpha O_2,$$

where the weighting between efficiency (maximum $\langle \tilde{B}_x \rangle$) and homogeneity was controlled by the dimensionless parameter α. In addition to this objective, the optimisation was constrained to produce a resonance frequency between 310 and 320 MHz. A target slightly above the Larmor frequency of 300 MHz was chosen since it is easy in practice to correct the resonance frequency downward by adding a small parallel capacitance. By contrast, increasing the resonance frequency of a resonator is very difficult.

The optimisation was carried out using the constrained optimisation by linear approximation (COBYLA) algorithm [22]. A typical optimisation trajectory is shown in Fig. 6. As shown in the top panel, the average normalised magnetic field starts to rise after the first few iterations. At the same time, the optimisation adapts the end capacitance value (not shown in the figure) to adjust the resonance frequency within the target band (shown in grey). The normalised magnetic field then gradually increases, converging to a value of about 2.27 mT/$\sqrt{\mathrm{W}}$ after 15 iterations. The trajectory of two out of the four optimisation

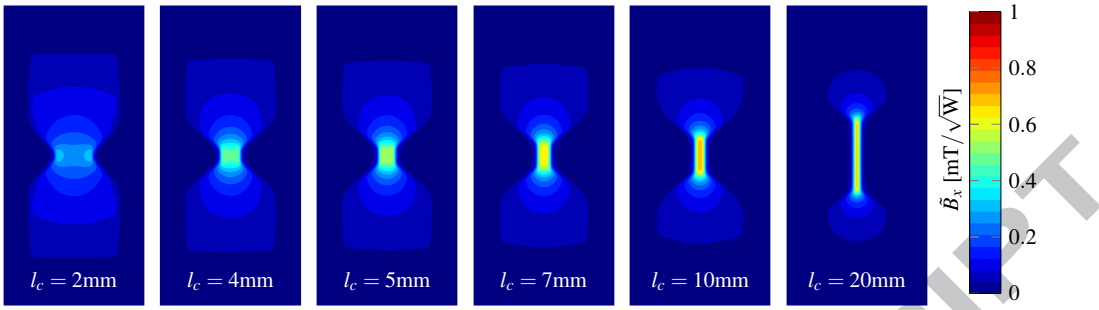

Figure 4: Field maps of the normalised magnetic field amplitude between resonator plates for resonators with varying constriction aspect ratio. Constriction areas is constant at 20 mm^2

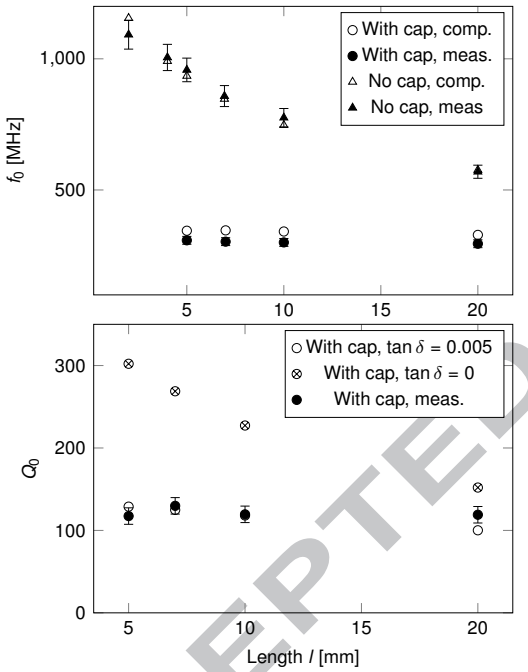

Figure 5: Validation of FEA model. Top: Predicted (open symbols) and experimental (filled symbols) resonance frequencies for open resonators (triangles) and for resonators tuned with end capacitors (circles). Bottom: predicted and measured resonator quality factors.

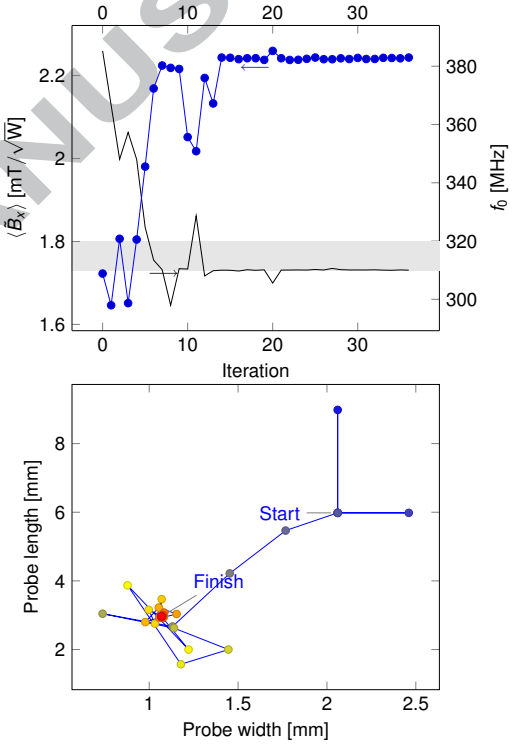

Figure 6: Top: convergence of the normalised average magnetic field $\langle \tilde{B}_x \rangle$ (blue dots). The resonance frequency (solid dark line) converges into the tolerance interval (grey band) within the first 10 iterations. Bottom: Optimisation trajectory of two out of the four optimisation variables.

Table 1: Optimisation parameters. Note that the product $l_s w_s$ was constrained to 5 mm^2.

Parameter	*Unit*	*initial*	*optimised*	
			$\alpha = 0$	$\alpha = 10$
l_s	[mm]	3.66	3.66	4.64
$w_s = 5\ \text{mm}^2/l_s$	[mm]	1.36	1.36	1.07
l_c	[mm]	6.00	2.97	5.20
w_c	[mm]	2.06	1.07	1.29
C_{end}	[pF]	35.00	57.40	52.98

variables is shown in the bottom panel of Fig. 6. The initial geometry (marked as "Start") combines a 6 mm × 2 mm constriction with a 3.66 mm × 1.36 mm sample chamber (cf. Tab. 1). As shown by the solid line in the top panel of Fig. 6, this leads to too high a resonance frequency of more than 380 MHz. The optimisation algorithm then proceeds to decrease both the length and the width of the resonator, while leaving the sample chamber largely unchanged. The resonance frequency is quickly brought into the target band by a combination of the higher inductance caused by the smaller resonator, and an increase in the end capacitance. After about 15 iterations, the result is essen-

tially converged.

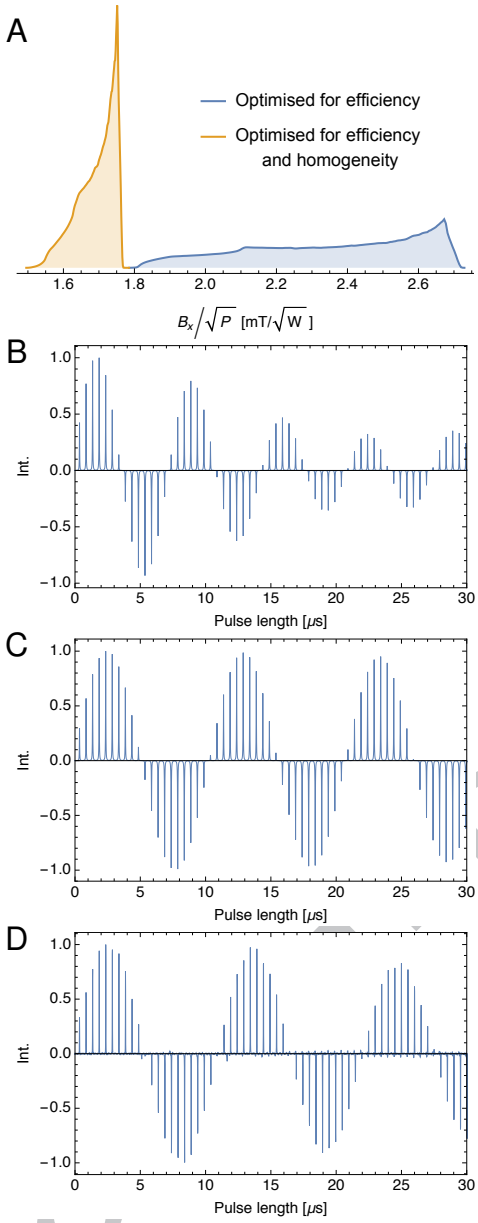

Figure 7: A: Histograms of normalised magnetic field amplitudes $\tilde{B}_x$ over the sample volume after optimisation with $\alpha = 0$ (efficiency, blue), and $\alpha = 10$ (efficiency and homogeneity, orange). B: computed nutation diagram from the histogram at $\alpha = 0$; C: computed nutation diagram at $\alpha = 10$; D: experimental nutation diagram from a resonator built to the geometry resulting from optimisation at $\alpha = 10$.

Fig. 7A shows a histogram of the RF magnetic field distribution over the sample volume resulting from the optimised structure. The optimisation has been run initially with $\alpha = 0$, thus optimising purely for efficiency. After convergence, α was set to 10, in order to obtain a balance between efficiency and homogeneity. As is obvious from Fig. 7A, this leads to a lower average field amplitude, but a substantially narrower field distribution. From these histograms, proton nutation diagrams can easily be predicted. The results are shown in Fig. 7B ($\alpha = 0$) and C ($\alpha = 10$). These nutation diagrams have been computed assuming a power input of 6.9 W. In the case of $\alpha = 0$, the length of a 2π pulse is about 7 μs, compared to 10.5 μs for the resonator obtained with $\alpha = 10$. At the same time, the more homogeneous field distribution is reflected in a much slower decay of the nutation signal. The ratio between the 90° and 810° amplitudes A_{810}/A_{90} amounts to more than 95% in the case of $\alpha = 10$, where it is less than 50% for $\alpha = 0$.

4.3. Performance Characterisation

As discussed in the experimental section, a resonator and corresponding microfluidic chip were built using the geometry optimised with $\alpha = 10$. The performance of this system was assessed using a solution of 150 mM sodium acetate in H_2O, with 10 mM DSS as a chemical shift reference. Fig. 8 shows a representative spectrum obtained in this way. The acetate sgnal at 1.4 ppm was used for the experimental nutation spectrum shown in Fig. 7D. Comparison with the corresponding simulated nutation diagram in Fig. 7C shows that the two are in excellent agreement. It should be noted that there are no adjustable parameters in this comparison; the transmitter power in the experiment has been set to the same value (−10 dB on the Bruker AVANCE spectrometer, corresponding to 6.89 W) that was used in the simulations. The length of a 360° pulse at 11 μs (corresponding to a probe efficiency of 34.6 kHz/ $\sqrt{\text{W}}$) is marginally longer in the experiment, but the difference is less than 0.5 μs. Also, the A_{810}/A_{90} ratio amounts to only 85%, compared to the simulated value of 95%. Both discrepancies are probably due to slight misalignment of the microfluidic chip and the probe assembly. Magnetic resonance images (not shown) reveal that the centres of the probe and the sample chamber were misaligned sideways by 20 . . . 50 μm due to manufacture tolerances.

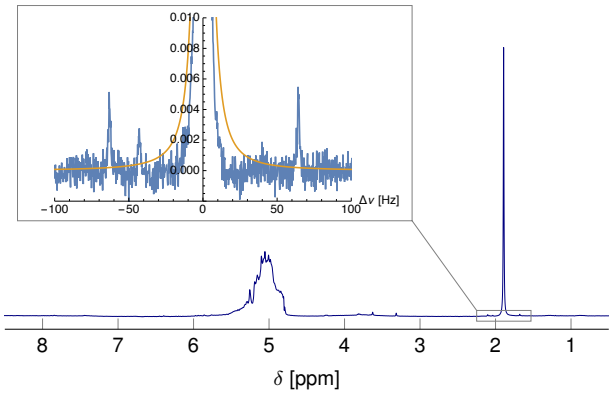

Figure 8: 1D NMR spectrum of 150 mM sodium acetate in H_2O, 32 scans with 90Hz water presaturation. Expanded region shows the line width at the base of the peak and the ^{13}C satellites.

The acetate spectrum shown in Fig. 8 demonstrates the excellent B_0 homogeneity offered by the optimised probe/chip system. The width of the acetate peak is 1.73 Hz at half height,

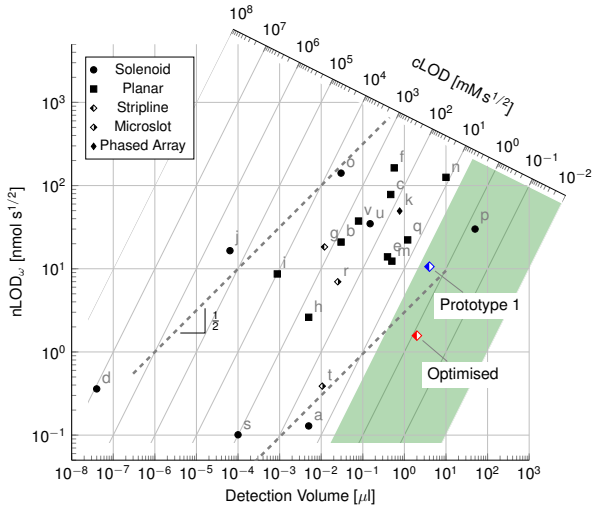

Figure 9: Plot comparing sensitivity of previously designed micro-NMR detectors. Letters a-t correspond to different authors as cited by Badilita *et al.* [5]. Data points u [23] and v [10] represent more recent work. The performance of the optimised probe presented here is shown in red, along with a similar, earlier prototype that had not been numerically optimised (blue).

and 16.45 Hz and 29.0 Hz at 0.55% and 0.11% height, respectively. The inset in Fig. 8 shows the details of the acetate peak base. The line shape is narrower than a Lorentzian peak with the same half width (orange solid line). A narrow peak base is particularly important for applications in metabolomics, where a large dynamic range is required to reliably quantify different metabolites with highly different concentrations. Fig. 10 illustrates this with a spectrum obtained in 256 scans from 2 μl of a DMEM cell growth medium. Peaks from several dozen metabolites are visible in the spectrum, with some of the most important ones labelled in the figure. Both the spectra in Fig. 8 and Fig. 10 have been recorded using standard pre-saturation water suppression with CW irradiation at 90 Hz amplitude; in the case of the DMEM medium spectrum, a perfect echo sequence [21] was used to reduce signals from compounds with high molecular weight.

Both spectra exhibit a broad feature slightly downfield from the water resonance. This is most likely due to contributions to the signal from areas of the chip/probe system that are quite far away from the active site, e.g., the access channels and inlets into the microfluidic device. In these regions, the B_0 field is somewhat different in magnitude, leading to an apparent downfield shift of the water resonance. As a result, the CW presaturation is not effective in suppressing these signals. Closer investigation of the exact origin of these signals is currently underway, with the goal of finding a probe/chip design that will minimise them.

The mass sensitivity of the optimised probe/chip system can be determined from the signal/noise ratio (SNR) of the acetate spectrum. The SNR of the acetate peak in the spectrum shown in Fig. 8 is 4200:1 for 16 scans, corresponding to a value of 740 for a single scan. From the SNR, the limit of detection can be computed as [5]

$$\mathrm{nLOD}_\omega = \frac{3n\sqrt{\Delta t}}{\mathrm{SNR}}, \tag{9}$$

where n is the number of sample spins precessing in the chosen resonance, and Δt is the total measurement time. Assuming a measurement time of 1.8 s per scan, which corresponds to the T_1 relaxation time of a typical metabolite such as glucose, and taking into account the number of protons that contribute to the acetate signal $n = 3 \cdot 150$ mM $\cdot$ 2 μl = 900 nmol, we obtain a limit of detection at 300 MHz of $\mathrm{nLOD}_\omega = 2.72$ nmol s$^{1/2}$. It is common practice to report sensitivities for micro-NMR detectors at a standard field strength of 14.1 T (600 MHz) to facilitate comprarison, using a scaling of $(\omega/\omega_0)^{\frac{7}{4}}$. The above limit of detection then amounts to

$$\mathrm{nLOD}_\omega^{600} = 1.57 \text{ nmol s}^{1/2}.$$

Fig. 9 compares the mass sensitivities of a wide variety of different micro-NMR detectors that have been reported in the literature. As is well known, the mass sensitivity is related to the size of the detector, as exemplified by the trend (dashed lines) in the data shown in Fig. 9. Clearly, the optimised resonator compares favourably with other systems of similar size, and is on par with the most sensitive solenoid capillary detectors that have been reported. For example, a stripline design with smaller sample volume of 0.012 μl affords a nLOD of 18.3 nmol s$^{1/2}$ (data point *g* [15]). Planar detector designs of a similar sample volume 0.4 [24], 0.5 [25], and 1.2 μl [8] also have higher mass limits of detection at 13.8, 12.3, and 22 nmol s$^{1/2}$ respectively (data points *c*, *f*, and *q*).

In the context of metabolomic studies, the mass sensitivity is not the only important consideration. Metabolites occur at concentrations that are limited by physiology; in most cases in the low mM range or less. Since Fig. 9 plots mass sensitivity versus detector size, the concentration limit of detection cLOD_ω can be represented by another axis, inclined by a slope of -1 with respect to the nLOD_ω axis. We somewhat arbitrarily set the limit of practicality for metabolomic studies at a concentration limit of detection of 5 mM $\sqrt{\text{s}}$, ensuring that species present at 0.1 mM concentration can be detected within less than 20 min of measurement time. The area where this condition is satisfied is shaded green in Fig. 9. The detector presented here lies well inside this region, whereas many other micro NMR detectors are not suitable for low-concentration studies, even though their mass sensitivity is superior. For example, a solenoid detector with an excellent nLOD of 0.1 nmol s$^{1/2}$ has been demonstrated (data point *s*, [26]). However, since the sample volume is only 100 pl, the cLOD is 1000 mM s$^{1/2}$, several orders of magnitude greater than that required for NMR at low concentrations.

The spectrum shown in Fig. 10, obtained from a mixture of DMEM cell growth medium with 10% fetal bovine serum (FBS) demonstrates the feasibility of meaningful metabolomic studies using the optimised probe/chip system.

5. Conclusions

We have optimised and demonstrated a new design of double micro stripline detector that is compatible with functional

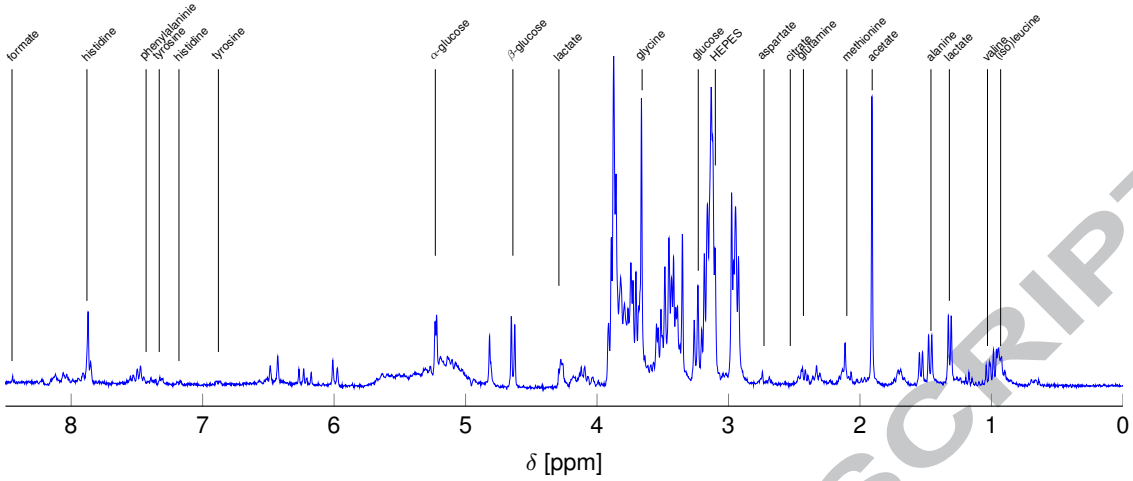

Figure 10: 1D NMR spectrum of DMEM cell growth medium solution supplemented with 10% fetal bovine serum, 256 scans with a total experiment time of 20 minutes.

microfluidic LoC devices, allowing non-invasive, sensitive observation of a 2 μl sample of sub-mM concentration. Its performance compares favourably with micro-NMR systems described by other authors. The optimisation has taken into account both the shape of the sample chamber and the RF resonator. Details of the geometry can make a big difference to the sensitivity of the probe. Different performance criteria, such as sensitivity and RF homogeneity, compete with each other, and a compromise must be chosen that fits the intended applications. While the present work has proved the principle of non-invasive NMR detection inside LoC devices with high sensitivity and resolution, the chip we have used is still rather primitive, and does not yet implement any active fluidic components such as continuous flow perfusion. Extensions of the current design are being developed in our group to allow active perfusion, controlled gas exchange and growth of cell populations on chip. Also, the probe will be fitted with an active temperature control system, in order to ensure optimum growth conditions during NMR measurements. Finally we are exploring extension of the current detector design in order to allow heteronuclear and multi-nuclear experiments.

6. Acknowledgements

This work has been supported by a Marie Curie Career Integration Grant to MU from the 7th EU Framework programme (Project uF-NMR). GF gratefully acknowledges the support of the iMR Centre for Doctoral Training funded by the UK Engineering and Science Research Council.

7. References

References

[1] J. El-Ali, P. K. Sorger, K. F. Jensen, Cells on chips., Nature 442 (7101) (2006) 403–11. doi:10.1038/nature05063.
URL http://dx.doi.org/10.1038/nature05063

[2] H. Andersson, A. van den Berg, Microfluidic devices for cellomics: a review, Sensors and Actuators B: Chemical 92 (3) (2003) 315–325. doi:10.1016/S0925-4005(03)00266-1.
URL http://www.sciencedirect.com/science/article/pii/S0925400503

[3] H. Kimura, T. Yamamoto, H. Sakai, Y. Sakai, T. Fujii, An integrated microfluidic system for long-term perfusion culture and on-line monitoring of intestinal tissue models., Lab on a chip 8 (5) (2008) 741–6. doi:10.1039/b717091b.
URL http://pubs.rsc.org/en/content/articlehtml/2008/lc/b717091b

[4] J. Clausell-Tormos, D. Lieber, J.-C. Baret, A. El-Harrak, O. J. Miller, L. Frenz, J. Blouwolff, K. J. Humphry, S. Köster, H. Duan, C. Holtze, D. A. Weitz, A. D. Griffiths, C. A. Merten, Droplet-based microfluidic platforms for the encapsulation and screening of Mammalian cells and multicellular organisms., Chemistry & biology 15 (5) (2008) 427–37. doi:10.1016/j.chembiol.2008.04.004.
URL http://www.sciencedirect.com/science/article/pii/S1074552108

[5] V. Badilita, R. C. Meier, N. Spengler, U. Wallrabe, M. Utz, J. G. Korvink, Microscale nuclear magnetic resonance: a tool for soft matter research, Soft Matter 8 (41) (2012) 10583. doi:10.1039/c2sm26065d.
URL http://xlink.rsc.org/?DOI=c2sm26065d

[6] S. S. Zalesskiy, E. Danieli, B. Blümich, V. P. Ananikov, Miniaturization of NMR systems: desktop spectrometers, microcoil spectroscopy, and "NMR on a chip" for chemistry, biochemistry, and industry., Chem. Rev. 114 (11) (2014) 5641–94. doi:10.1021/cr400063g.
URL http://dx.doi.org/10.1021/cr400063g

[7] K. Ehrmann, M. Gersbach, P. Pascoal, F. Vincent, C. Massin, D. Stamou, P.-A. Besse, H. Vogel, R. S. Popovic, Sample patterning on NMR surface microcoils., J. Magn. Reson. 178 (1) (2006) 96–105. doi:10.1016/j.jmr.2005.08.018.
URL http://www.sciencedirect.com/science/article/pii/S1090780705

[8] H. Ryan, S.-H. Song, A. Zaß, J. Korvink, M. Utz, Contactless NMR spectroscopy on a chip., Anal. Chem. 84 (8) (2012) 3696–702. doi:10.1021/ac300204z.
URL http://dx.doi.org/10.1021/ac300204z

[9] H. G. Krojanski, J. Lambert, Y. Gerikalan, D. Suter, R. Hergenröder, Microslot NMR probe for metabolomics studies., Anal. Chem. 80 (22) (2008) 8668–72. doi:10.1021/ac801636a.
URL http://www.ncbi.nlm.nih.gov/pubmed/18939856

[10] N. Spengler, A. Moazenzadeh, R. C. Meier, V. Badilita, J. G. Korvink, U. Wallrabe, Micro-fabricated Helmholtz coil featuring disposable microfluidic sample inserts for applications in nuclear magnetic resonance, J. Micromechanics Microengineering 24 (3) (2014) 034004. doi:10.1088/0960-1317/24/3/034004.
URL http://stacks.iop.org/0960-1317/24/i=3/a=034004

[11] O. G. Gruschke, N. Baxan, L. Clad, K. Kratt, D. von Elverfeldt, A. Peter, J. Hennig, V. Badilita, U. Wallrabe, J. G. Korvink, Lab on a chip

phased-array MR multi-platform analysis system., Lab Chip 12 (3) (2012) 495–502. doi:10.1039/c2lc20585h.
URL http://pubs.rsc.org/en/Content/ArticleHTML/2012/LC/C2LC20585H

[12] K. Göbel, O. G. Gruschke, J. Leupold, J. S. Kern, C. Has, L. Bruckner-Tuderman, J. Hennig, D. von Elverfeldt, N. Baxan, J. G. Korvink, Phased-array of microcoils allows MR microscopy of ex vivo human skin samples at 9.4 T., Skin Res. Technol. 21 (1) (2015) 61–8. doi:10.1111/srt.12157.
URL http://www.ncbi.nlm.nih.gov/pubmed/25066249

[13] D. L. Olson, T. L. Peck, A. G. Webb, R. L. Magin, J. V. Sweedler, High-Resolution Microcoil 1H-NMR for Mass-Limited, Nanoliter-Volume Samples, Science (80-.). 270 (5244) (1995) 1967–1970. doi:10.1126/science.270.5244.1967.
URL http://www.sciencemag.org/cgi/doi/10.1126/science.270.5244.1967

[14] E. Harel, C. Hilty, K. Koen, E. E. McDonnell, A. Pines, Time-of-Flight Flow Imaging of Two-Component Flow inside a Microfluidic Chip, Phys. Rev. Lett. 98 (1) (2007) 017601. doi:10.1103/PhysRevLett.98.017601.
URL http://link.aps.org/doi/10.1103/PhysRevLett.98.017601

[15] P. J. M. van Bentum, J. W. G. Janssen, A. P. M. Kentgens, J. Bart, J. G. E. Gardeniers, Stripline probes for nuclear magnetic resonance., J. Magn. Reson. 189 (1) (2007) 104–13. doi:10.1016/j.jmr.2007.08.019.
URL http://www.sciencedirect.com/science/article/pii/S1090780707002546

[16] J. Bart, A. J. Kolkman, A. J. Oosthoek-de Vries, K. Koch, P. J. Nieuwland, H. J. W. G. Janssen, J. P. J. M. van Bentum, K. a. M. Ampt, F. P. J. T. Rutjes, S. S. Wijmenga, H. J. G. E. Gardeniers, A. P. M. Kentgens, A microfluidic high-resolution NMR flow probe., J. Am. Chem. Soc. 131 (14) (2009) 5014–5. doi:10.1021/ja900389x.
URL http://www.ncbi.nlm.nih.gov/pubmed/19320484

[17] D. Hoult, R. Richards, The signal-to-noise ratio of the nuclear magnetic resonance experiment, Journal of Magnetic Resonance (1969) 24 (1) (1976) 71–85. doi:10.1016/0022-2364(76)90233-X.
URL http://www.sciencedirect.com/science/article/pii/002223647690233X

[18] D. M. Pozar, Microwave Engineering, 4th Edition, Wiley, Hoboken, New Jersey, 2012.

[19] M. A. Leontovich, On the approximate boundary conditions for the electromagnetic field on the surface of well conducting bodies, in: B. W. Vvedensky (Ed.), Investigations of Radio Waves, Moscow: Acad. of Sci. USSR, 1948, pp. 5–12.

[20] S. Yuferev, N. Ida, Surface Impedance Boundary Conditions: A Comprehensive Approach, CRC Press, 2010.

[21] J. A. Aguilar, M. Nilsson, G. Bodenhausen, G. A. Morris, Spin echo NMR spectra without J modulation, Chem. Commun. 48 (6) (2012) 811–813.

[22] M. J. Powell, A direct search optimization method that models the objective and constraint functions by linear interpolation, in: Advances in optimization and numerical analysis, Springer, 1994, pp. 51–67.

[23] R. C. Meier, J. Höfflin, V. Badilita, U. Wallrabe, J. G. Korvink, Microfluidic integration of wirebonded microcoils for on-chip applications in nuclear magnetic resonance, J. Micromechanics Microengineering 24 (4) (2014) 045021. doi:10.1088/0960-1317/24/4/045021.
URL http://iopscience.iop.org/0960-1317/24/4/045021/article/

[24] J. D. Trumbull, I. K. Glasgow, D. J. Beebe, R. L. Magin, Integrating microfabricated fluidic systems and NMR spectroscopy., IEEE Trans. Biomed. Eng. 47 (1) (2000) 3–7. doi:10.1109/10.817611.
URL http://www.ncbi.nlm.nih.gov/pubmed/10646271

[25] R. R. A. Syms, M. M. Ahmad, I. R. Young, D. J. Gilderdale, D. J. Collins, Microengineered needle micro-coils for magnetic resonance spectroscopy, J. Micromechanics Microengineering 16 (12) (2006) 2755–2764. doi:10.1088/0960-1317/16/12/032.
URL http://stacks.iop.org/0960-1317/16/i=12/a=032

[26] D. A. Seeber, R. L. Cooper, L. Ciobanu, C. H. Pennington, Design and testing of high sensitivity microreceiver coil apparatus for nuclear magnetic resonance and imaging, Rev. Sci. Instrum. 72 (4) (2001) 2171. doi:10.1063/1.1359190.
URL http://link.aip.org/link/RSINAK/v72/i4/p2171/s1&Agg=doi

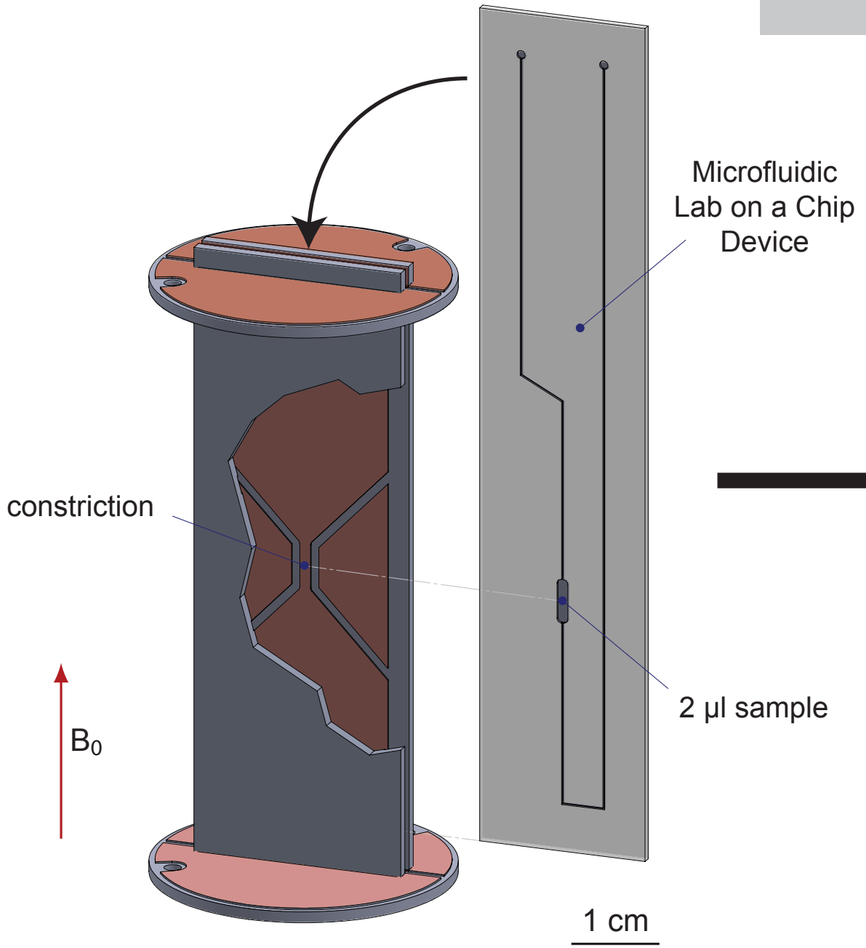

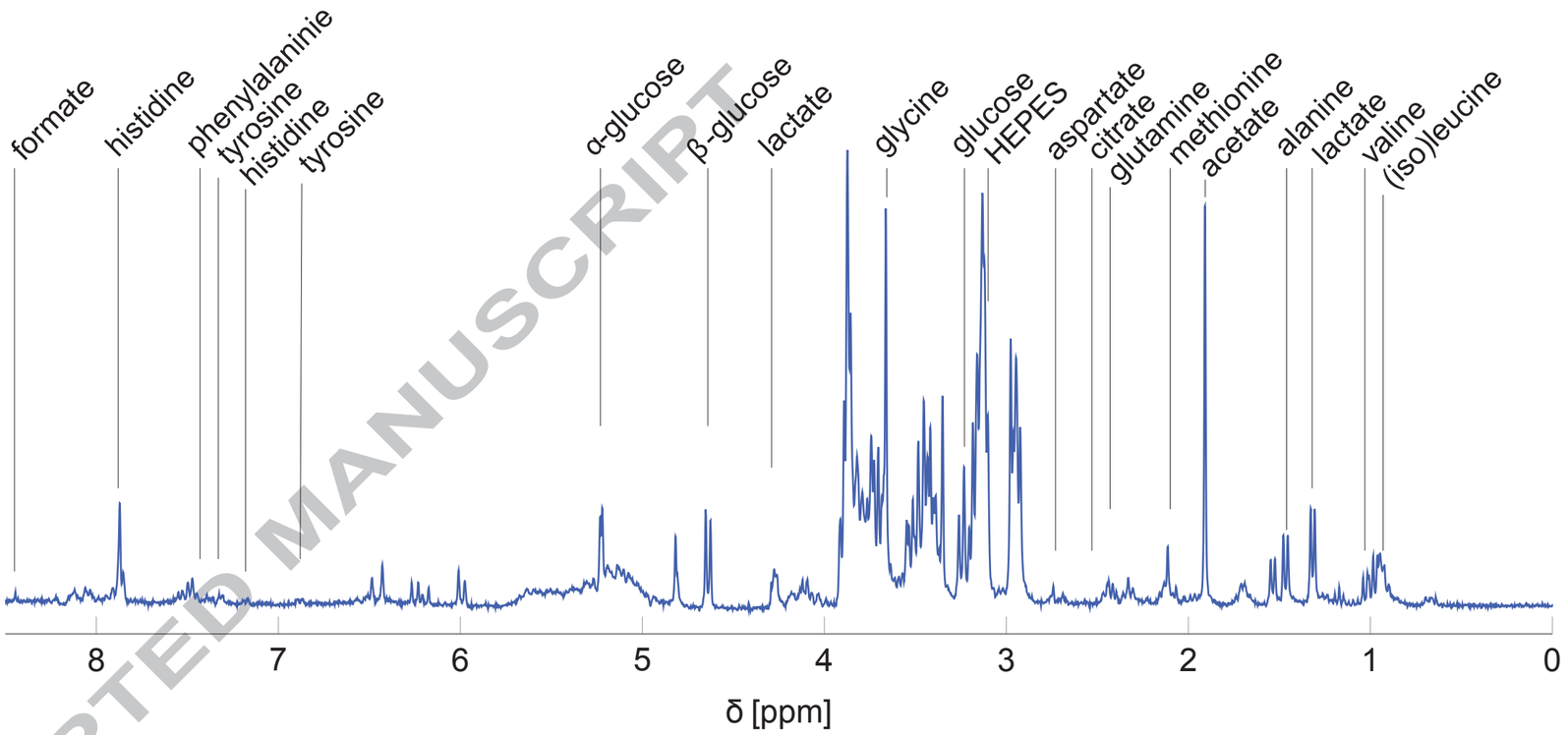

- We present a double-stripline probe that accommodates planar microfluidic devices.
- Finite element analysis is used to optimise the detector and sample volume geometry.
- Sensitivity of the detector is quantified by normalised limit of detection, $nLOD_{\omega} = 1.57$ nmol $s^{1/2}$.
- The probe's sensitivity allows observation of a 2 μl sample of sub-mM concentration.
- The spectral resolution is better than 1.75 Hz at 7 T, with excellent line shape.